

Cluster Dynamics with HETDEX at $z < 0.5$ - I: Simulated Performance, Mass Recovery, and Limits to Cosmology

Steven Boada,^{1*} C. Papovich,¹ R. Wechsler,^{2,3} T. S. Li,¹ K. Gebhardt,⁵ J. DeRose,² E. Rozo,^{2,4} E. S. Rykoff²

¹George P. and Cynthia Woods Mitchell Institute for Fundamental Physics and Astronomy, and Department of Physics and Astronomy, Texas A&M University, College Station, TX, 77843-4242, USA

²Kavli Institute for Particle Astrophysics and Cosmology, Department of Physics, Stanford University, Stanford, CA 94305, USA

³Department of Particle Physics and Astrophysics, SLAC National Accelerator Laboratory, Menlo Park, CA 94025, USA

⁴Department of Physics, University of Arizona, Tucson, AZ 85721, USA

⁵Department of Astronomy, The University of Texas at Austin, Austin, TX 78712, USA

Accepted XXX. Received YYY; in original form ZZZ

ABSTRACT

The distribution of massive clusters of galaxies depends strongly on the total cosmic mass density, the mass variance, and the dark energy equation of state. As such, measures of galaxy clusters can provide constraints on these parameters and even test models of gravity, but only if observables of clusters can lead to accurate estimates of their total masses. Here, we carry out a study to investigate the ability of a blind spectroscopic survey to recover accurate galaxy cluster masses through their velocity dispersion. We focus on the Hobby Eberly Telescope Dark Energy Experiment (HETDEX), which will employ the new VIRUS integral field unit (IFU) spectrograph, over 420 degree² on the sky with a 1/4.5 fill factor. The instrument covers the blue/optical portion of the spectrum (3500–5500 Å), allowing surveys with VIRUS to measure redshifts for a large sample of galaxies out to $z < 0.5$ based on their absorption features or [O II] $\lambda 3727$ emission (and Lyman- α over $1.9 < z < 3.5$). We use a detailed mock galaxy catalog from a semi-analytic model to simulate surveys observed with VIRUS, including: (1) a blind, HETDEX-like survey with an incomplete but uniform spectroscopic selection function; and (2) IFU surveys that target clusters directly, obtaining spectra of all galaxies in a VIRUS-sized field. For both surveys, we include realistic uncertainties from galaxy magnitude and line-flux limits. We benchmark both surveys against spectroscopic observations with “perfect” knowledge of galaxy line-of-sight velocities. Using both observing strategies, we produce cluster mass probability density functions $P(M_{200c}|\vec{x})$ of a cluster mass (M_{200c}) as a function of an observable parameter or set of observable parameters, \vec{x} , where we consider cases of where $\vec{x} = \{\sigma\}$, $= \{\sigma, z\}$, and $= \{\sigma, z, N_{gal}\}$ for velocity dispersion, σ , redshift, and number of observed galaxies, N_{gal} . **This sentence will summarize how well HETDEX will do, and how that might be improved with Targeted observations.**

1 INTRODUCTION

Our ability to perform precision cosmology with clusters of galaxies has reached a critical point. The widely accepted Λ CDM model of cosmology makes explicit predictions about the mass function of galaxy clusters in the universe. Measuring this mass function across many redshifts, in turn, provides constraints on the cosmology. Today, large-area sky surveys are providing observations of large numbers of clusters, but systematics in deriving cluster masses dominate the error budget (e.g., Sehgal et al. 2011; Planck Collaboration 2013; Bocquet et al. 2015). To place further constraints on the Λ CDM model of cosmology, we must decrease these systematics.

As mass is not a direct observable, a lot of work is under-

way to characterize galaxy cluster masses with an observable feature of galaxy clusters. The goal is to constrain, as best possible, $P(M|z, \vec{x})$ the probability (P) that a galaxy cluster of given mass (M), located at redshift (z) determined using an observable parameter or parameters (\vec{x}). Generally, cluster mass calibrations fall into two distinct camps, simulation based and direct or statistical calibration.

One could use various simulations to attempt to calibrate this observable–mass relation (e.g., Vanderlinde et al. 2010; Sehgal et al. 2011). However, the primary challenge to this method is the incomplete understanding of the baryonic physics which take place in galaxy cluster environments. While there have been (and continue to be) many improvements in the accuracy and power of simulations it is doubtful that in the coming years they will reach the accuracy level

required where the observable–mass relation is dominated only by statistics (Weinberg et al. 2013).

The second broad camp is the direct calibration of cluster masses. This recipe has two distinct but not always independent tracks. The “direct” method uses direct observations of a small set of clusters and then uses known mass estimators, including X-ray temperatures and luminosities (e.g., Mantz et al. 2010; Rykoff et al. 2014), cosmic microwave background (CMB) observations (e.g., Vanderlinde et al. 2010; Sehgal et al. 2011), optical richness (e.g., Abell 1958; Rykoff et al. 2012) or weak lensing (WL; e.g. Rozo et al. 2010) as examples, which provide a “true” mass. This directly calibrates the observable–mass relation which is then applied to a much larger sample. The complications lie in that the “true” masses are, in fact, estimations, and the methods used to recover these cluster masses are subject to their own limitations. X-ray based cluster masses assume hydrostatic equilibrium (e.g., Mantz et al. 2015) which may only be valid for a very small number and range of cluster masses. The Sunyaev-Zel’dovich Effect (SZE; Sunyaev & Zeldovich 1972), which uses the up-scattering of CMB photons to estimate cluster masses, provides accurate estimations of mass, but the ability to detect low mass galaxy clusters is currently limited by technology (e.g., Carlstrom et al. 2002). WL estimates are, in principle, correct in the mean, but they suffer from signal-to-noise requirements, limiting their usefulness in low mass clusters, and potentially suffer from line-of-sight effects as WL is sensitive to all mass along the line-of-sight. Virial mass estimators which determine the cluster mass based on the motions of the member galaxies (e.g., Ruel et al. 2014; Sifón et al. 2015b) are promising in that it is a direct measurement of the depth of clusters potential well, but suffer from systematics due to cluster formation physics which disrupts the velocity field.

The statistical method of determining galaxy cluster mass relies not on direct measurements of individual clusters but the calibration of observables for the entire sample which correlate with cluster mass. One example is the spatial clustering of the galaxy clusters themselves (e.g., Baxter et al. 2016). See Weinberg et al. (2013) for a comprehensive review. In practice, it will be a combination of the three methods touched on that will provide the most reliable determination of cluster masses.

Large-area sky surveys, both on going and planned, are revolutionizing cluster cosmology using a large range of wavelengths. The South Pole Telescope (SPT; Carlstrom et al. 2011) and the Atacama Cosmology Telescope (ACT; Swetz et al. 2011) are discovering many clusters through the SZE. Optically, the on going Dark Energy Survey (DES; The Dark Energy Survey Collaboration 2005) and planned Large Synoptic Survey Telescope (LSST; LSST Dark Energy Science Collaboration 2012) will identify many thousands of clusters to much lower masses than is possible with SZE measurements. However, regardless of the discovery method used, spectroscopic followup is needed to further constrain $P(M|z, X)$. But as the cluster dataset grows to many tens of thousands of clusters individual followup becomes increasingly impractical. Therefore, large spectroscopic surveys are needed to more fully constrain the observable–mass relation of clusters.

The Hobby Eberly Telescope Dark Energy eXperiment (HETDEX; Hill et al. 2008) is a trailblazing effort to ob-

serve high-redshift large scale structures using cutting edge wide-field integral field unit (IFU) spectrographs. Designed to probe the evolution of the dark energy equation of state etched onto high redshift ($z > 2$) galaxies by the Baryon Acoustic Oscillations (BAO) (Eisenstein et al. 2005) in the first moments of the universe, the survey will observe two fields for a total of 420 degree² (300 degree², Spring field and 120 degree², Fall field). Tuned to find Ly α emitting (LAE) galaxies at $1.9 < z < 3.5$, HETDEX expects to find 800,000 LAEs, and more than one million [O II] emitting galaxies at $z < 0.5$ masquerading as high-redshift galaxies (Acquaviva et al. 2014).

While a large portion of the $\sim 10^6$ interloping lower redshift galaxies will be field (not associated with a bound structure) galaxies, the large area covered by HETDEX is expected to contain as many as 50 Virgo-sized (halo mass $> 10^{15} M_{\odot}$) clusters at $z < 0.5$. The near-complete spectroscopic coverage allows an unprecedentedly detailed look at a very large number of clusters ranging from group scales to the very massive. In addition to the recovery of accurate dynamical masses, detailed investigations of the dynamical state of the clusters is possible.

It is unclear how a blind spectroscopic survey with an IFU will effect the recovery of galaxy cluster dynamical properties. Unlike many previous large cluster surveys (e.g., Milvang-Jensen et al. 2008; Robotham et al. 2011; Sifón et al. 2015b) which use multi-object spectrographs, the Visible Integral-Field Replicable Unit Spectrograph (VIRUS; Hill et al. 2012) used by HETDEX samples the sky in a uniform but sparse way which could excluded member galaxies which would otherwise be included. Secondly, it is not straightforward to use spectroscopic redshifts predominately from emission-line galaxies to interpret the kinematic and dynamical states of the clusters.

This work plans to address these concerns in the following ways. We create and evaluate a HETDEX like selection “function” of galaxies over a similarly large portion of the sky and use well adopted techniques to recover the dynamical properties, such as velocity dispersion and cluster mass. In addition to standard techniques of cluster mass estimation, we investigate probability based and machine learning based approaches of cluster mass prediction. We compare these results to a series of targeted galaxy cluster observations, where each member galaxy is assumed to be observed. Each of these observations use realistic uncertainties from galaxy magnitude and line-flux limits. These strategies will better allow future work to predict the number and types of galaxy clusters which should be observed with VIRUS during both the HETDEX survey portion and through targeted follow up observations.

We begin in Section 2 by giving an overview of what data is used, how it is created, and how we make our “observations.” Details about the determination of cluster parameters, velocity dispersion, total mass, etc., are discussed in Section 3. Next, we present the results of our study in Section 4 and discuss their implications in Section 5. Finally we summarize our findings in Section 6. A followup to this work (Boada 2016) will investigate how the techniques developed here will work in practice.

Throughout this paper, we adopt the following cosmological model: $\Omega_{\Lambda} = 0.714$, $\Omega_M = 0.286$, $\sigma_8 = 0.82$ and $H_0 = 70 \text{ km s}^{-1} \text{ Mpc}^{-1}$ (taken from the Buzzard catalogs;

see below), assume a Chabrier initial mass function (IMF; Chabrier 2003), and use AB magnitudes (Oke 1974).

2 DATA AND MOCK OBSERVATIONS

In this section, we describe the data products and the techniques used to replicate the HETDEX survey. We use the information from a large mock galaxy catalog enhanced by the emission line properties of galaxies in the SDSS to create a realistic “sky” and “observe” it with a HETDEX-like observing strategy.

2.1 The Buzzard Mock Catalogs

The Buzzard mock galaxy catalogs cover 398.49 degree^2 between $4^h < RA < 6^h$ and $-61^\circ < DEC < -41^\circ$ and are derived from a combination of Sub-halo Abundance Matching (ShAM) and ADDSEDS (Adding Density Dependent Spectral Energy Distributions) tied to an in house n-body cosmological simulation. A brief description of the catalog creation is described as follows. The initial conditions are generated with a second-order Lagrangian perturbation theory using 2LPTIC (Crocce et al. 2006). Dark matter (DM) n-body simulations are run using LGADGET-2 (a version of GADGET-2; Springel 2005). The DM halos are identified using the ROCKSTAR halo finder (Behroozi et al. 2013) which also calculates halo masses.

Galaxy M_r luminosities are added to the velocity peaks using ShAM (Reddick et al. 2013), and ADDSEDS assign luminosities in the other bands. A M_r -density-SED relation is created using a SDSS training set, and for each mock galaxy the SED of a randomly selected training set galaxy which has a similar M_r and density is assigned. The result is a mock catalog containing 238 million galaxies with $r < 29$ mag and $z \leq 8.7$.

The catalog information, used in this study, is broken into two large portions. The “truth” files contain the characteristics of each individual galaxy, such as right ascension (RA), declination (DEC), redshift (z), observed and rest-frame magnitudes, and many others. The “halo” files contain information for individual halos, to which many individual galaxies may belong. This includes five estimations of dynamical mass, RA, DEC, z , three dimensional velocity dispersion, and many others. However, the catalogs do not include information for emission lines. We supplement the catalogs by generating this information; the process is described in Section 2.2.

We investigate the accuracy of the halo mass distribution by comparing the cumulative number density of halos above a mass (M_{200c}) threshold to the halo mass function (HMF) of Tinker et al. (2008). We calculate the HMF at central redshifts of 0.1, 0.2, and 0.4 using HMFALC (Murray et al. 2013) and compare it galaxies in a redshift window of $\Delta z \pm 0.01$. We find a very good agreement between the predicted HMF and the observed distribution of clusters.

2.2 Conditional [O II] Flux Probability Distribution Functions

We use the SDSS DR12 (Alam et al. 2015) catalogs to assign [O II] emission line strengths to the galaxies in the Buzzard

catalog. We use 503113 galaxies from $z = 0.05 - 0.2$, which are selected with no redshift warning, and place each galaxy on a color-magnitude diagram (CMD) of M_r and $g - r$; see the left panel of Figure 1.

To assign an [O II] luminosity to each galaxy in our catalog, we place the catalog galaxies on the same CMD and select all SDSS galaxies in a small 2D ($M_r, g - r$) bin around the galaxy. We extract all of the SDSS galaxies inside that bin and create a histogram of their [O II] luminosities, the right panel of Figure 1. Using a slice sampling technique (Neal 1997) we assign the catalog galaxy an [O II] luminosity based on the distribution of SDSS galaxies in that bin. In very few cases (1.3% of galaxies) do the $g - r$ and M_r magnitudes of the galaxies in the Buzzard catalog not overlap with the distributions in SDSS. For these objects, we assign them zero [O II] flux, but this has no impact on our analysis. For catalog galaxies with have very few ($1 \leq N < 10$) SDSS galaxies in their respective bin, we assign it the mean [O II] flux.

Figure 1 illustrates this process. The numbered boxes in the left panel show two bins ($M_r, g - r = -17.7, 0.49$ and $M_r, g - r = -21.4, 1.24$) in the CMD of $0.05 < z < 0.2$ SDSS galaxies. The right panel shows the Log [O II] luminosity distribution functions, $p([O II]|M_r, g - r)$, which we use to assign [O II] luminosity to each object. The luminosity is then converted into an [O II] flux through

$$F = \frac{L}{4\pi D_L} \quad (1)$$

where D_L is the luminosity distance (e.g., Hogg 1999).

2.3 HETDEX

There are quite a few words copied from Casey’s SHELA paper. HETDEX will perform a blind survey which will measure the redshifts of 8×10^5 Ly α emitting galaxies (LAEs) between $1.9 < z < 3.5$ using a collection of 78 wide-field IFUs spectrographs covering the wavelength region 3500 – 5500 Å at $R \sim 750$ (Hill et al. 2008). The goal of these observations will be to provide sub-percent level measurements of the Hubble expansion parameter and the angular diameter distance at $z \sim 2$ via the large scale distribution of galaxies in the redshift range of HETDEX. The result will be a significant constraint on the evolution of dark energy that is competitive with (and independent of) values based on surveys of the Ly α forest.

The entire HETDEX survey will cover 420 degree^2 with a $1/4.5$ filling factor over two fields: a $\sim 300 \text{ degree}^2$ northern field, and a $\sim 140 \text{ degree}^2$ equatorial region. The 10σ detection limit for these spectra will be $3.5 \times 10^{-17} \text{ erg s}^{-1} \text{ cm}^{-2}$ at 5000 Å, or equivalently for continuum objects, $g = 21.9$ mag. The spectral coverage allows for the detection of [O II] ($\lambda\lambda 3727, 3729$) emitters to $z \sim 0.5$ and Ca H ($\lambda 3968.5$) and K ($\lambda 3933.7$) absorption features to $z \sim 0.4$.

The HETDEX IFU pattern is illustrated in Figure 2 and consists of 78 IFUs, which are comprised of 448 optical fibers subtending a $50'' \times 50''$ region on the sky (Kelz et al. 2014). The inter-IFU spacing is also $50''$ spanning a total area of $16' \times 16'$ on the sky. The individual IFUs have a fill-factor of $1/3$, which will be completely filled with three dithers of the telescope at each pointing.

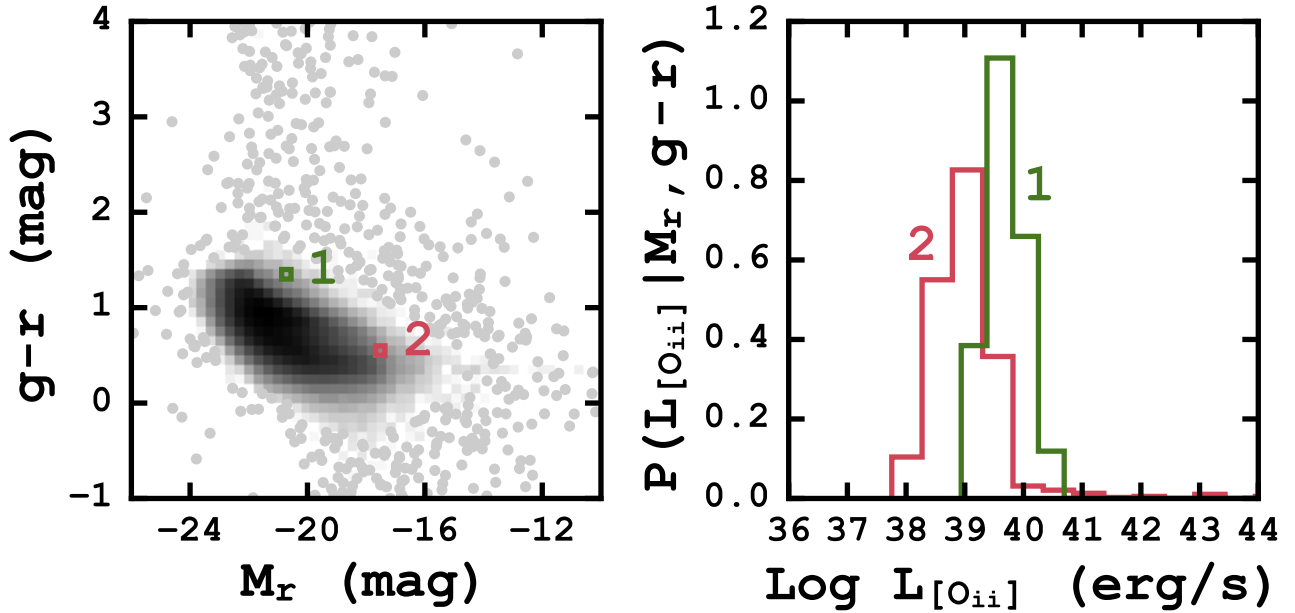


Figure 1. *Left:* CMD of 503113 $z < 0.2$ galaxies taken from the SDSS DR12 where the shading scales with the density of points. The two colored boxes show regions containing potential catalog galaxies. *Right:* Probability histograms of the Log [O II] luminosity for the SDSS galaxies located in the two highlighted regions on the right. The [O II] luminosities are assigned to catalog galaxies from slice sampling the probability histogram and converted to fluxes using the redshift of each galaxy.

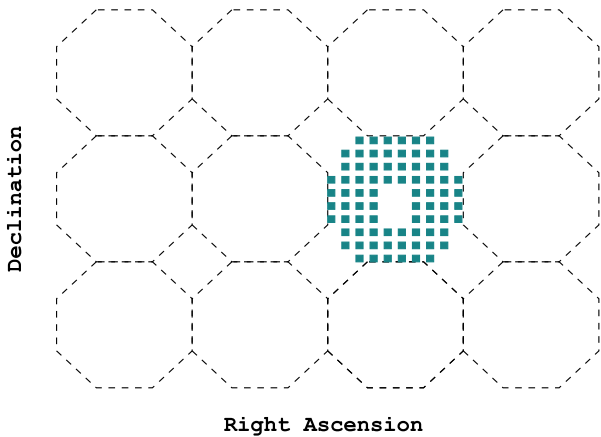


Figure 2. Representative observation tiling scheme for the HETDEX $16' \times 16'$ pointings. Each colored square is a single VIRUS IFU and the dashed octagons approximate the size of a single observation. See the text for more details.

2.4 Mock Observations

This means that when selecting galaxies from the Buzzard catalog we assume an observation for all galaxies lying within a colored, IFU square in Figure 2. Galaxies which lie between the IFUs are missed, as well as the galaxies which lie between the pointings, as there is no overlap between one pointing and the next. To cover the 398.49 degree^2 field of the Buzzard catalog we require 5370 pointings where 0.015 degree^2 of each pointing is covered by an IFU. The total area

of the sky covered by an IFU is 80.80 degree^2 which gives a filling factor of $1/4.65$, slightly decreased from the expected filling factor of $1/4.5$.

In this work we consider two separate observing strategies, Targeted and Survey-like. The Targeted observations use “direct” observations where each cluster is targeted individually, and every cluster member galaxy is assumed to be observed. The Survey observations mimic the HETDEX observation pattern across the sky, where no cluster is directly targeted and not all cluster member galaxies are observed. Both of these observations have HETDEX-like galaxy detection thresholds, and for comparison we also include a set of Targeted observations with “perfect” knowledge. Perfect observations assume no detection threshold, if a cluster member galaxy is observed, it is also detected. This provides an important best-case scenario, and differs from the true cluster properties because the cluster properties are still calculated. These observations provide three levels of quality with “Perfect knowledge” being the highest and Survey being the lowest.

3 RECOVERY OF PARAMETERS

In the following subsections, we outline the methods we use to derive the dynamical properties of the galaxy clusters in our sample. The following is, in many cases, a subset of the available methods to derive any single parameter. The specific choice of method may improve or diminish the accuracy of the recovered parameter, but the methods chosen were to facilitate comparison with other observational studies (e.g., Boada 2016).

3.1 Cluster Redshift

The accurate determination of the cluster redshift (z_c) is crucial to the reliability of all following measurements. An incorrect cluster redshift introduces error into the measured line-of-sight velocity (LOSVD) and corresponding dispersion, which, in turn, contributes to errors associated with dynamical mass and radius.

In simple terms, the cluster redshift is the mean of the redshifts of all galaxies associated with the cluster, where the mean is the first moment of the velocity (redshift) distribution function $p(z)$. In practice, the first moment is strongly subject to outliers, so we rely instead on the biweight location estimator (Beers et al. 1990) through¹:

$$C_{BI} = M + \frac{\sum_{|u_i| < 1} (x_i - M)(1 - u_i^2)^2}{\sum_{|u_i| < 1} (1 - u_i^2)^2} \quad (2)$$

where x_i are the individual redshifts, M is the median redshift and u_i is given by:

$$u_i = \frac{(x_i - M)}{cMAD} \quad (3)$$

MAD is the median absolute deviation, also defined in Beers et al. (1990), and c is the a tuning constant. We choose $c = 6$ (the suggested value) which balances computational speed and location accuracy.

Although this work assumes that we know each galaxy's redshift to infinite precision, in practice, we find a simple weighted mean provides a reliable estimate of z_c when there are uncertainties on the individual galaxy redshifts.

3.2 Line-of-Sight Velocity Dispersion

We calculate the LOSVD to each galaxy, where

$$\text{LOSVD} = c \frac{z - z_c}{1 + z_c} \quad (4)$$

and c is the speed of light in km s^{-1} , z is the redshift of the individual galaxy, and z_c is the overall cluster redshift described in the previous section.

We follow the maximum likelihood method of ? to estimate the line-of-sight velocity dispersion (LOSVD). We maximize the probability function

$$p(\{v_1, \dots, v_N\}) = \prod_{i=1}^N \frac{1}{\sqrt{2\pi(\sigma_i^2 + \sigma_p^2)}} \exp\left[-\frac{1}{2} \frac{(v_i - \langle u \rangle)^2}{(\sigma_i^2 + \sigma_p^2)}\right] \quad (5)$$

where σ_p , $\langle \mu \rangle$, and σ_i is the LOSVD, the average radial velocity and the error on the individual LOSVs respectively, using a Monte Carlo Markov Chain (MCMC) sampler (EMCEE²; Foreman-Mackey et al. 2013) which is based on affine-invariant ensemble sampler (see Goodman & Weare 2010 for details on affine-invariant samplers). We draw twenty thousand samples from the posterior probability distribution using simple priors, $\langle \mu \rangle$ lies between the maximum and minimum LOSVD and $0 < \sigma_p < 1400 \text{ km s}^{-1}$. We set the upper limit on the LOSVD as the LOSVD corresponding to a $10^{16} M_\odot$ cluster at $z \sim 0.0$, higher mass than any expected

cluster. When the full distribution of LOSVDs is not used, the final LOSVD is quoted as the median value of the posterior probability distribution with 68% error bars defined as the 16th and 84th percentiles of the same distribution.

In principle, a single statistic such as the biweight scale estimator or the gapper estimator (both from Beers et al. 1990) with many bootstrap resamplings could be used to construct a distribution of σ_p . In simple tests where the values of both σ_p and $\langle \mu \rangle$ are known, the 68% error bars derived from the MCMC method give slightly better results with the true LOSVD value bracketed by the error bars in $\sim 68\%$ of the cases versus $\sim 57\%$ with bootstrapping and a single statistic. In addition, we prefer the maximum likelihood method for its straight forward treatment of the errors in the LOSVD measurements, which will become important in the practical application to real data (e.g., Boada 2016).

3.3 Estimates of Cluster Mass

3.3.1 Power Law Based Method

The relationship between the LOSVD and cluster dynamical mass has been the focus of several many (e.g., Evrard et al. 2008; Saro et al. 2013; Sifón et al. 2013; van der Burg et al. 2014), where the relationship for the mass enclosed by r_{200c} takes the form

$$M_{200c} = \frac{10^{15}}{h(z)} \left(\frac{\sigma_{1D}}{A_{1D}} \right)^{1/\alpha} M_\odot \quad (6)$$

with $A_{1D} = 1177 \pm 4.2 \text{ km s}^{-1}$ (Munari et al. 2013; referred to as σ_{15} in Evrard et al. 2008 and other works), $\alpha = 1/3$, $h(z) = H(z)/100$, and σ_{1D} is the LOSVD of the velocity tracers (dark matter particles, subhalos or galaxies). $H(z) = H_0 E(z)$ and $E(z) = \sqrt{\Omega_m(1+z^3) + \Omega_\Lambda}$.

A growing body of work suggests that there is a significant difference in the observed LOSVD depending on the velocity tracers used. Specifically, while there is little difference between using galaxies and their host DM subhalos, there is a significant over estimation of the LOSVD when using galaxies/subhalos compared to DM particles (Munari et al. 2013). We follow other works (e.g., Kirk et al. 2015; Sifón et al. 2015a) using the scaling relation, given in Equation 6 from Munari et al. (2013) to facilitate comparisons with other observational studies, which rely on galaxies as tracers.

3.3.2 Other Estimates of Dynamical Mass – Introduction

In this section we use two methods to predict the mass of a cluster based on other observables. Often the cluster mass is estimated based on a single observable, X-ray temperature, LOSVD, richness and others (see Section 1 for referenced examples). Here we combine many observables to attempt to correct the mass inferred solely from the velocity dispersion. The first method is traditional “probability based” where we marginalize over a series of observables to find the most probable cluster mass. The second is based on a machine learning (ML) algorithm which attempts to infer the relationship between the observables and the desired output, the cluster mass. Both of these methods are examples

¹ Implemented as part of the ASTLIB Python library. See <http://astlib.sourceforge.net>

² <http://dan.iel.fm/emcee/current/>

of supervised learning algorithms where the relationship between the observable parameters and the target parameter (the cluster mass) are both known.

As with any predictive analysis it is important to test the model on data that the model has not seen before. This prevents over-fitting. In the following subsections we take all of the observed clusters, our full sample, split them, and generate a *training* and *testing* set (e.g., Ripley 2007; Xu et al. 2013; Ntampaka et al. 2015b,a; Acquaviva 2016). Traditionally, the training set is a set of data used to infer possibly predictive relationships. The test set of data is then used to assess the correctness of the predictive relationship. Our data is randomly split into 70% training and 30% testing. We follow the ML convention and refer to the individual clusters in each set as a “sample”, and the parameters associated with the cluster (z , LOSVD, mass, etc.) as “features”.

3.3.3 Probability Based

For internal consistency between this and the ML based method we use 70% of the clusters to establish a conditional probability density of $p(M_{200c}|\vec{x})$ which we then use as the mass probability density for the remaining clusters with similar features. In this way we, “train” the probability density using the existing simulated data, and apply it to the “test” sample (the remaining 30% of the data not used as the “training” set).

Figure 3 shows all of the one (marginalized probability) and two (joint probability) dimensional projections of the posterior probability distributions of the features of the training data.

The conditional probability of the mass $P(M_{200c}|\vec{x} = \{x_1, x_2, \dots\})$ is determined by taking a slice through the joint probability distributions in bins centered on the desired value. The slices, shown by the colored bars in Figure 3, are centered on $\sigma = 400 \text{ km s}^{-1}$ and $z = 0.17$. The distribution of cluster mass contained in the three dimensional bin given by the intersection of these slices is $P(M_{200c}|\vec{x} = \{\sigma = 400 \text{ km s}^{-1}, z = 0.17\})$.

For the clusters making up the *test* sample the mass is unknown (it is what we are trying to predict) but the other features are known. To determine the mass probability distribution of a test cluster, $P(M_{200c})$, we combine the conditional probability distribution, $P(M_{200c}|\vec{x})$, created previously with the probability distribution of σ through Equation 7.

$$P(M_{200c}) = \int P(M_{200c}|\vec{x}) P(\sigma) d\sigma \quad (7)$$

The expected mass is determined by calculating the first moment of the probability density. This becomes our “predicted” cluster mass, M_{pred} .

$$M_{pred} = \int M_{200c} P(M_{200c}) dM_{200c} \quad (8)$$

The confidence interval associated with this prediction can be estimated two ways. First, by calculating the second moment of the probability density through

$$\text{Var} = \int (M_{200c} - M_{pred})^2 P(M_{200c}) dM_{200c} \quad (9)$$

or by drawing many samples from $P(M_{200c})$ and calculating

the values at the 16th and 84th percentile. In practice we find that both methods produce similar results for a large number of trials. Therefore, we quote predicted masses as the most probable mass given by Equation 8 and associated 68% error estimated through Equation 9.

3.3.4 Machine Learning Based

The cluster mass estimation in this section relies on a ML technique known as an ensemble method, where many estimators are created by a single learning method with the goal of improved generalization and robustness compared to a single estimation. Ensemble methods (e.g., Caruana & Niculescu-Mizil 2006) come in two general flavors. Averaging methods average (hence the name) the estimators to produce a single prediction. Boosting estimators build estimates sequentially by attempting to address poor performing estimators in each previous step, hence “boosting” the predictive power.

Here we use an averaging ensemble learning method known as a forest of randomized decision trees, often shortened to just random forest (RF; Tin Kam Ho 1995, 1998). Decision trees can be visualized a flow chart where forks are the branches of the tree. The path along the tree is decided by the values of the feature(s) at each branch. RF estimators use a random subset of the training set at each fork to decide which path should be followed. The final prediction is then the average of all the final predictions from the trees. We use RF regression methods as implemented in SCIKIT-LEARN (Pedregosa et al. 2012).

We note the subtle distinction that the ML method generates “prediction intervals” between observed and derived quantities (rather than “confidence intervals”). A prediction interval is an estimate of the interval encompassing future observations, with a certain probability. And, unlike confidence intervals, which describe uncertainties on the different moments of a population, a prediction interval is unique to each prediction. In many regression analyses, such as linear fitting, the prediction intervals are based on underlying assumptions of normally distributed residuals. However, RF estimators do not have any such assumptions and require special treatment.

The prediction intervals here are based on the general method of quantile regression forests (Meinshausen 2006). The general idea is that all response variables are recorded, not just the mean. Then the prediction can be returned as the full conditional probability distribution of all responses, which allows us to generate the prediction intervals. The 68% prediction interval is determined by calculating the 16th and 84th percentile of the full conditional probability distribution.

4 RESULTS

Here we explore the cluster member recovery rate and mass estimates for the two observing strategies, Targeted, and Survey. Targeted observations are direct observations of a cluster where each cluster member galaxy, above the detection thresholds (see Section 2.4), is observed. Survey observations mimic the HETDEX observation strategy such that no cluster is directly observed, and only the cluster member

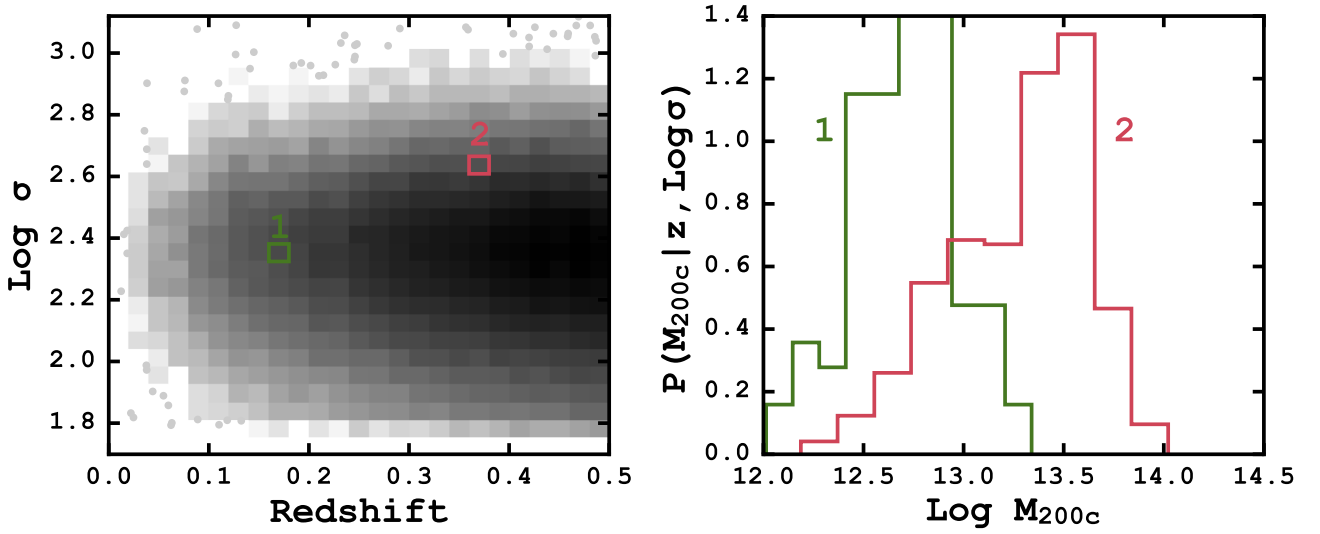


Figure 3. Corner plot of the *training* data with features σ and z . The corner plots shows all of the one and two dimensional posterior probability distributions used to determine the correct cluster mass. The colored rectangles, which have been enlarged for clarity, show the slices needed to create a conditional probability distribution of the mass, $P(M_{200c}|\vec{x})$. See text for a complete description.

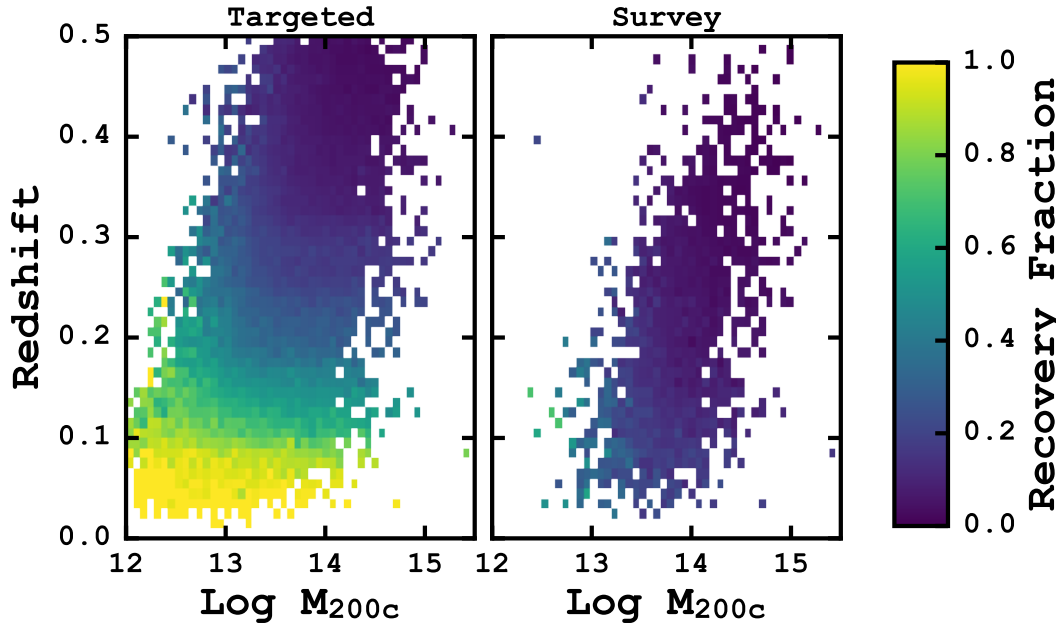


Figure 4. Recovery fractions (N_{obs}/N_{True}) of cluster member galaxies as a function of redshift and true cluster mass for the Targeted and Survey observing strategies. We have applied HETDEX-like observational limits on the cluster galaxy detection, and require at least five galaxies to be detected for a cluster to be recovered. The solid lines are the median values and the shaded regions represent the 68% scatter. The significant decline in galaxies observed with the Survey strategy is due to gaps in the VIRUS IFU.

galaxies above the detection threshold and within an IFU (see Figure 2) are observed. We discuss the accuracy of cluster dynamical mass derived from both the power law scaling relation (see Equation 6) and through the probability and ML methods.

We compare the results from the Targeted and Survey observing strategies to the results of a “Perfect” survey,

where the redshift (and therefore LOSV) of each galaxy in the cluster is known perfectly).

4.1 Recovery of Cluster Members

As discussed in Section 2.4 the observational constraints place limits on the total number of clusters member galax-

ies expected to be recovered. Knowing these limits will provide important information for potential future follow up or Targeted observations. Figure 4 shows the recovery fraction of member galaxies, the number of observed galaxies divided by the number of actual galaxies (N_{obs}/N_{True}), as a function of both redshift and cluster mass. We require a detection of ($N_{obs} \geq 5$) galaxies for a cluster to be detected and included in this figure. As expected, the Targeted observing strategy where the individual clusters are targeted through several dithers to ensure near complete coverage, performs significantly better than the Survey observing strategy across all redshifts and cluster masses. With Perfect knowledge, recovery fraction would be unity across all redshifts and cluster masses.

For the clusters recovered as a function of redshift (left panel of Figure 4), there are two effects at work. The decrease in recovery fraction with increasing redshift is a magnitude effect. We check this by limiting the cluster galaxy detection by absolute magnitude which increases the recovery fraction to $> 70\%$ at all redshifts, implying the decline is a result of the apparent magnitude cluster galaxy detection threshold. The second key feature is the strong decline in clusters recovered from Survey observations. This is due to gaps in the VIRUS IFU. The median recovery fraction in Survey observations is almost exactly 4.5 times less than the Targeted median recovery fraction. As the total filling factor of the Survey increases the two lines will converge.

The recovery rate as a function of cluster mass, right panel of Figure 4, shows that of the low mass clusters we detect ($N_{obs} > 5$), we observe the majority of the galaxies. This also shows a rapid decrease in the detection fraction, which can again be explained by considering absolute magnitudes instead of apparent magnitudes, as above. Also, high mass clusters are rare, so in order to detect them we must probe a large volume of space. The higher redshift cluster members suffer from the limiting apparent magnitude and suppress the recovery fraction at fixed mass. If we were to limit the Survey to $z < 0.2$ we find the recovery fraction of clusters, at all masses, increases substantially, and we find a much more consistent detection fraction across all masses.

4.2 Mass estimates

In this section we discuss the how accurately we recover the true cluster mass from a set of observations. We report on three methods, the power law based approach (Eq. 6), the probability based approach (Section 3.3.3) and the ML based method (Section 3.3.4). For each method we consider observations with Perfect knowledge, Targeted observations and Survey observations.

Because it represents the best possible scenario, the Perfect knowledge observations should serve as baseline to compare the power law based, probability based and ML cluster mass recovery methods. And, while there are many possible metrics to evaluate performance, we compute two: the average bias (given in Table 1)

$$\mu_{bias}(y, \hat{y}) = \frac{1}{N} \sum_{i=1}^N (\hat{y}_i - y_i). \quad (10)$$

where y are the true values and \hat{y} are the predicted values,

and the scatter about the bias (given in Table 2)

$$\sigma_{bias}(y, \hat{y}, \mu_{bias}) = \left[\frac{1}{N-1} \sum_{i=1}^N (\hat{y}_i - y_i - \mu_{bias})^2 \right]^{1/2} \quad (11)$$

with N clusters in a given bin. Both metrics evaluate how closely the ensemble of predicted cluster masses are to the true cluster masses, and in both cases values closer to zero are better.

We begin with the Perfect knowledge observations. These observations are of the same clusters as the Targeted observations but without any observational limits. The cluster masses predicted by Equation 6 gives the following results. For clusters with masses between $\text{Log } M/M_{\odot} = 13 - 15.5$, we find $\mu_{bias} = 0.15 \pm 0.002$ dex and $\sigma_{bias} = 0.24 \pm 0.001$. The scatter in recovered masses can be attributed to both physical and numerical effects. The presence of any in-falling matter onto lower mass clusters can introduce a significant amount of substructure, leading to artificial biasing of the measured LOSVD to higher values, increasing the predicted mass (e.g., Ntampaka et al. 2015b). Also, as the number of cluster galaxies decreases the LOSVD PDF is poorly sampled leading to poorly recovered cluster masses due to numerical effects. The cluster masses presented here are recovered using the best possible conditions, where we have Perfect knowledge of the cluster membership. In reality, the mass recovery levels presented in this section represent an upper bound (the best) on the accuracy achievable through this method.

For the Targeted and Survey observations the power law predicted cluster masses give $\mu_{bias} = 0.13 \pm 0.003$ dex, $\sigma_{bias} = 0.37 \pm 0.002$ and $\mu_{bias} = 0.11 \pm 0.009$ dex, $\sigma_{bias} = 0.36 \pm 0.006$, respectively. So for the clusters that we detect with Survey observations, we obtain similar levels of accuracy as to the Targeted observations, on the average. This does not mean that the Survey observations cannot be improved by Targeted observations. In fact, when comparing only the galaxies which overlap between the two samples the bias and scatter of the Targeted observations is significantly decreased as more cluster member galaxies are detected, better sampling the LOSVD PDF. The Targeted observations performs similarly on the average because many lower mass clusters are included in the sample, increasing the bias of the overall sample.

In both Figures 5 and 6, we show the predicted (M_{pred}) versus true (M_{200c}) cluster masses for each of the two observing strategies. In each panel the solid black line is the 1:1 relationship, the solid purple line is the median recovered mass for the Targeted observing, and the turquoise, dashed line is the median recovered mass for the HETDEX-like observations. The shaded regions are the 68% scatter around the median values (the 16% and 84% quartiles). For reference we also show the median masses recovered with Perfect knowledge as a dash-dotted orange line. The lower panels show the fractional cluster mass error defined as:

$$\epsilon = (M_{pred} - M_{200c})/M_{200c} \quad (12)$$

where M_{pred} is the predicted cluster mass and M_{200c} is the true cluster mass.

Qualitatively, the top panels of Figures 5 and 6 show that both the probability based and ML based methods out perform (closer to the black 1:1 relation) the power law

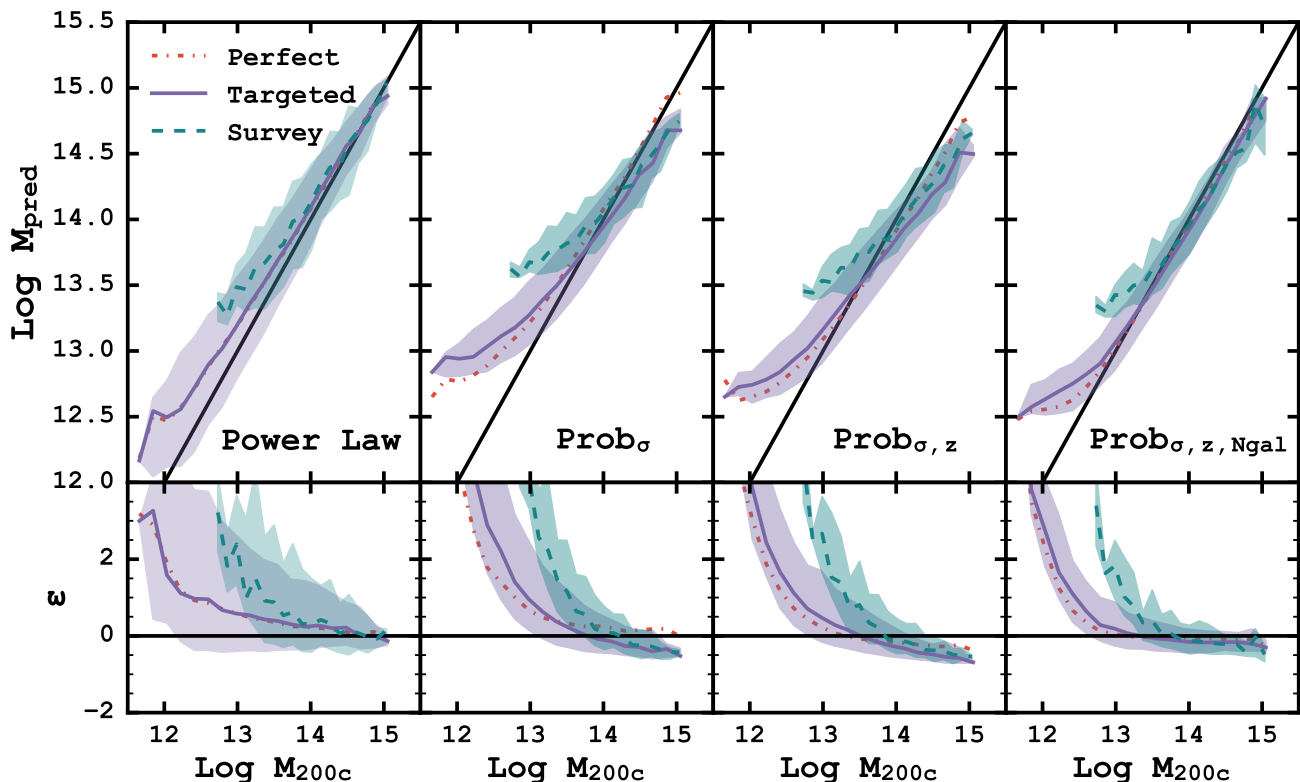


Figure 5. Mass predictions for the power law scaling relation (Equation 6) and the probability based technique with different input features as a function of true cluster mass. The bottom row of panels shows the fractional error (Equation 12) also as a function of true cluster mass. The solid black line shows the 1:1 relation. The solid, colored line is the median predicted mass for the Targeted observing, and the colored, dashed line is the median recovered mass for the HETDEX-like observations. The shaded regions represent the 68% scatter around the median values.

method when taking advantage of other cluster observables (z , N_{gal} , etc.). Generally, we find that the single parameter probability and ML methods perform significantly poorer than the power law method, especially at low cluster masses. When combined with the cluster redshift, the predicted cluster masses are improved, even though it is unclear exactly why the additional information should effect the predicted cluster mass. The final addition of the number of observed galaxies, N_{gal} acts as a type of richness estimate, and significantly improves both the bias and the amount of scatter in the predicted masses.

We quantify the bias and scatter for all of the different cluster mass recovery strategies and observing methods in Table 1 and Table 2. It serves as a type of look up table for future cluster observations with HETDEX. The columns represent bins of predicted galaxy cluster mass and the individual values show the bias and scatter of the true cluster mass. The three horizontal sections represent perfect, Targeted and Survey observations respectively. So, for example, if a cluster mass is predicted using the $ML_{\sigma,z}$ method and Targeted observations to be $\text{Log } M/M_{\odot} = 13 - 13.5$, it is biased upward by 0.03 ± 0.00 dex.

A few caveats apply to the numbers given in Table 1 and Table 2. While we provide corrections for cluster masses above $10^{15} M_{\odot}$, they are estimated from only a handful of

objects, and do not constitute a representative sample of clusters. On the opposite end of the cluster mass spectrum, Survey observations of low mass clusters are incomplete for two potential reasons. There are very few, if any, clusters detected with Survey observations below $10^{12} M_{\odot}$. Missing corrections above $10^{12} M_{\odot}$ in the probability based methods are due to low number statistics and an inability to sample the cluster mass PDF well enough to assign cluster mass predictions.

4.3 Significance of Training Sample Cosmology Choice

All simulations (including that used for Buzzard) use specific choices for cosmological parameters. When using simulation data to train ML methods, we incorporate all of those assumptions into the learned feature associations. This could lead to a notable bias when applying the ML method to data (real or simulated) which has significantly different cosmological assumptions.

We turn to the Millennium simulation where the underlying cosmological assumptions differ substantially from Buzzard. The Millennium simulation adopts a flat cosmological model based of the values derived from the Two-degree Field Galaxy Redshift Survey (Colless et al. 2001) and the

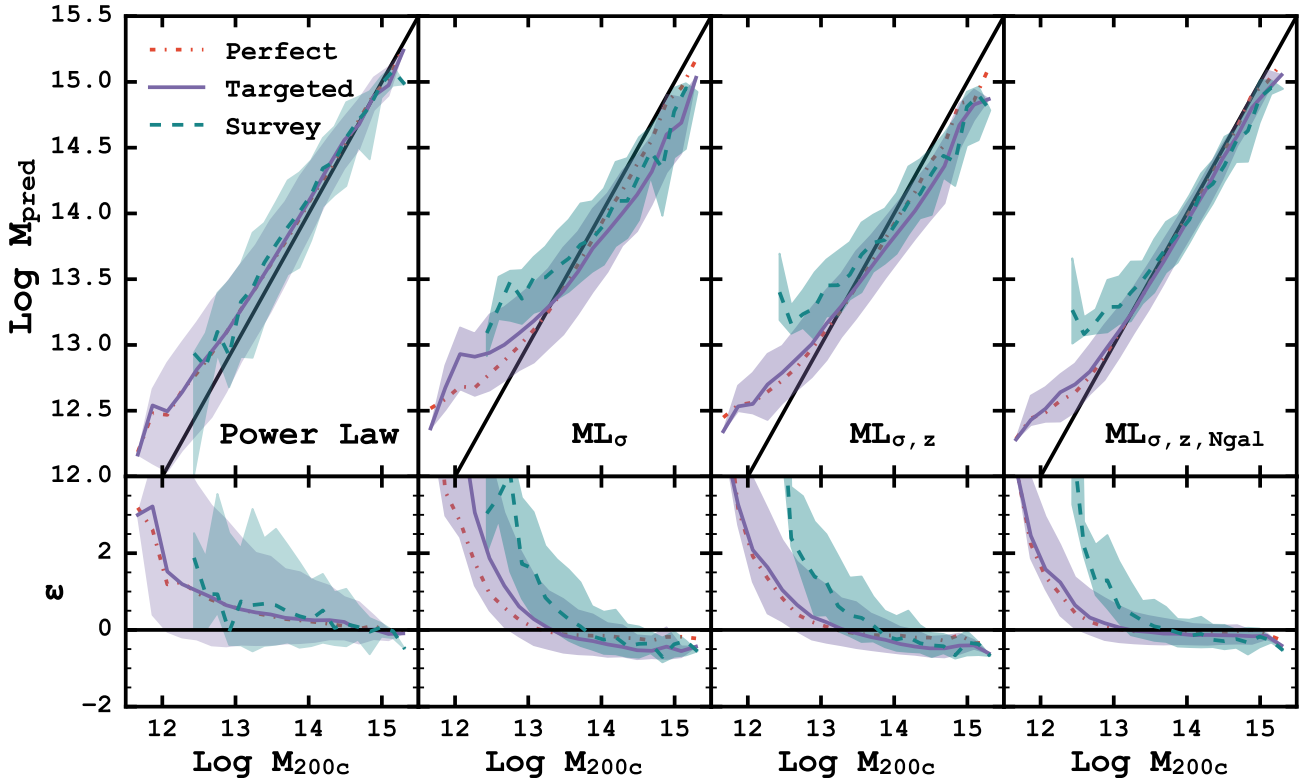


Figure 6. Mass predictions for the power law scaling relation (Equation 6) and the ML based technique with different input features as a function of true cluster mass. The bottom row of panels shows the fractional error (Equation 12) also as a function of true cluster mass. The solid black line shows the 1:1 relation. The solid, colored line is the median predicted mass for the Targeted observing, and the colored, dashed line is the median recovered mass for the HETDEX-like observations. The shaded regions represent the 68% scatter around the median values.

first year data of the *Wilkinson Microwave Anisotropy Probe* (WMAP; [Spergel et al. 2003](#)): $\Omega_{\Lambda} = 0.75$, $\Omega_M = 0.25$, $\sigma_8 = 0.9$, $n_s = 1$ and $H_0 = 73 \text{ km s}^{-1} \text{ Mpc}^{-1}$. The clusters in Millennium provide a testing sample to understand how a training sample derived from Buzzard will impact the mass recovery on a wholly new dataset.

We repeat our analysis using cluster halo and galaxy catalogs from the Millennium simulation ([Springel et al. 2005](#)) obtained via querying the Millennium online database³ ([Lemson & The Virgo Consortium 2006](#)). The Millennium simulation tracks 2160^3 dark matter particles of $8.6 \times 10^8 h^{-1} M_{\odot}$ inside a comoving $500 (h^{-1} \text{ Mpc})^3$ box from $z = 127$ to 0. The halo catalogs are created using a friends-of-friends algorithm (e.g., [Turner & Gott, J. R. 1976](#)) with linking length, $b = 0.2$. The halos are populated with galaxies using a semi-analytical model described in [Croton et al. \(2006\)](#); [De Lucia et al. \(2006\)](#); [De Lucia & Blaizot \(2007\)](#).

We select 4806 clusters, comprised of 623,663 galaxies, at $0.02 < z < 0.5$ and $M > 10^{13} M_{\odot}$, and apply the same data processing as with the Buzzard galaxies. We begin by assigning each galaxy an [O II] flux value (see Section 2.2), and “observe” each galaxy using realistic (see Section 2.4) observational limits. After recovering 3750 clusters which

have at least five galaxies observed, we calculate the LOSVD of each cluster as in Section 3.2.

We conduct our test in two ways. Both use the ML methods (see Section 3.3.4) to predict the cluster masses of the Millennium clusters, but each test uses a different training set. First, we use the full set of clusters detected in the Buzzard catalogs (14,000 clusters with $M > 10^{11} M_{\odot}$) to train the ML. Second, the Millennium clusters are split into training-testing samples. This provides a test case where we have different cosmological choices between the training and testing samples, and the same cosmological assumptions in both samples.

The top panel of Figure 7 shows the ML predicted cluster masses for the ~ 4000 Millennium clusters as a function of true cluster mass. The orange (Millennium) and green (Buzzard) colors indicate the two different training samples. The median (solid and dashed lines) predicted cluster masses show similar trends regardless of the training data set used. Figure 7’s bottom panel shows the fraction error (Equation 12) also as a function of true cluster mass. The large amount of scatter (the shaded area) in the fractional error for the Buzzard trained predictions is due to the training set including clusters with masses below the $M = 10^{13} M_{\odot}$ threshold for the Millennium clusters. This allows the ML method to predict masses which can be significantly dif-

³ <http://gavo.mpa-garching.mpg.de/Millennium/>

Table 1. Mean bias ($M_{pred} - M_{200c}$) for different bins of predicted cluster mass. This table shows the bias in the predicted cluster mass for the perfect (top section), Targeted (middle section), and Survey (bottom section) observations in different predicted mass bins. The different mass recovery strategies are given in the leftmost column. It can be used to understand how the predicted cluster mass differs from the true cluster masses. Positive numbers indicate the predicted cluster mass over estimates when compared to the true cluster mass.

Method		Bins – Log M_{pred}							
		11.5 – 12	12 – 12.5	12.5 – 13	13 – 13.5	13.5 – 14	14 – 14.5	14.5 – 15	15 – 15.5
Perfect Observations									
Prob Based	Power Law	0.49 ± 0.09	0.28 ± 0.02	0.23 ± 0.01	0.16 ± 0.00	0.11 ± 0.00	0.07 ± 0.00	0.02 ± 0.01	−0.07 ± 0.04
	σ	0.87 ± 0.04	0.53 ± 0.01	0.32 ± 0.01	0.16 ± 0.00	0.10 ± 0.00	0.07 ± 0.00	0.05 ± 0.01	−0.18 ± 0.06
	σ, z	0.76 ± 0.04	0.42 ± 0.01	0.17 ± 0.00	0.01 ± 0.00	−0.06 ± 0.00	−0.11 ± 0.01	−0.14 ± 0.01	−0.38 ± 0.13
	σ, z, N_{gal}	0.65 ± 0.03	0.28 ± 0.01	0.04 ± 0.01	−0.02 ± 0.00	−0.02 ± 0.00	−0.05 ± 0.01	−0.22 ± 0.12	−6.62 ± 3.06
ML Based	Power Law	0.49 ± 0.09	0.28 ± 0.02	0.23 ± 0.01	0.16 ± 0.00	0.11 ± 0.00	0.07 ± 0.00	0.02 ± 0.01	−0.07 ± 0.04
	σ	0.69 ± 0.05	0.36 ± 0.01	0.15 ± 0.01	−0.02 ± 0.00	−0.07 ± 0.00	−0.09 ± 0.01	−0.11 ± 0.01	−0.12 ± 0.07
	σ, z	0.62 ± 0.05	0.33 ± 0.01	0.12 ± 0.00	−0.01 ± 0.00	−0.06 ± 0.00	−0.09 ± 0.00	−0.11 ± 0.01	−0.19 ± 0.05
	σ, z, N_{gal}	0.51 ± 0.04	0.23 ± 0.01	0.05 ± 0.00	−0.02 ± 0.00	−0.02 ± 0.00	−0.02 ± 0.00	−0.02 ± 0.01	−0.08 ± 0.03
Targeted Observations									
Prob Based	Power Law	0.49 ± 0.08	0.27 ± 0.02	0.20 ± 0.01	0.13 ± 0.01	0.10 ± 0.01	0.09 ± 0.01	0.02 ± 0.01	−0.08 ± 0.03
	σ	1.02 ± 0.03	0.66 ± 0.01	0.40 ± 0.00	0.17 ± 0.00	0.02 ± 0.00	−0.08 ± 0.01	−0.19 ± 0.01	−0.35 ± 0.10
	σ, z	0.85 ± 0.05	0.49 ± 0.01	0.25 ± 0.00	0.08 ± 0.00	−0.06 ± 0.00	−0.21 ± 0.02	−0.35 ± 0.02	−0.59 ± 0.12
	σ, z, N_{gal}	0.70 ± 0.03	0.37 ± 0.01	0.13 ± 0.00	0.01 ± 0.00	−0.05 ± 0.00	−0.12 ± 0.02	−0.44 ± 0.18	−4.45 ± 2.81
ML Based	Power Law	0.49 ± 0.08	0.27 ± 0.02	0.20 ± 0.01	0.13 ± 0.01	0.10 ± 0.01	0.09 ± 0.01	0.02 ± 0.01	−0.08 ± 0.03
	σ	0.76 ± 0.07	0.54 ± 0.01	0.26 ± 0.01	0.01 ± 0.00	−0.13 ± 0.00	−0.23 ± 0.01	−0.33 ± 0.02	−0.32 ± 0.03
	σ, z	0.66 ± 0.03	0.37 ± 0.01	0.17 ± 0.01	0.03 ± 0.00	−0.09 ± 0.00	−0.21 ± 0.01	−0.31 ± 0.02	−0.28 ± 0.05
	σ, z, N_{gal}	0.57 ± 0.03	0.28 ± 0.01	0.09 ± 0.00	−0.01 ± 0.00	−0.05 ± 0.00	−0.08 ± 0.00	−0.07 ± 0.01	−0.14 ± 0.05
Survey Observations									
Prob Based	Power Law	0.53 ± 0.04	0.30 ± 0.02	0.16 ± 0.01	0.07 ± 0.01	0.01 ± 0.02	−0.09 ± 0.05
	σ	0.77 ± 0.03	0.42 ± 0.01	0.18 ± 0.01	−0.03 ± 0.01	−0.18 ± 0.02	−0.39 ± 0.08
	σ, z	0.61 ± 0.03	0.29 ± 0.01	0.08 ± 0.01	−0.11 ± 0.01	−0.38 ± 0.12	−0.48 ± 0.10
	σ, z, N_{gal}	0.48 ± 0.04	0.18 ± 0.01	0.02 ± 0.01	−0.08 ± 0.01	−0.50 ± 0.20	−8.81 ± 3.02
ML Based	Power Law	...	0.06 ± 0.46	0.17 ± 0.07	0.17 ± 0.02	0.13 ± 0.01	0.07 ± 0.01	0.01 ± 0.02	−0.09 ± 0.05
	σ	...	0.58 ± 0.10	0.54 ± 0.04	0.24 ± 0.02	0.03 ± 0.01	−0.17 ± 0.01	−0.26 ± 0.03	−0.30 ± 0.10
	σ, z	...	1.02 ± 0.20	0.42 ± 0.04	0.19 ± 0.01	0.03 ± 0.01	−0.14 ± 0.01	−0.25 ± 0.02	−0.31 ± 0.10
	σ, z, N_{gal}	...	0.91 ± 0.26	0.39 ± 0.03	0.12 ± 0.01	−0.00 ± 0.01	−0.08 ± 0.01	−0.14 ± 0.02	−0.21 ± 0.08

ferent, whereas the Millennium training set does not include $M < 10^{13} M_{\odot}$ clusters, which reduces the scatter of the predicted masses.

Based on these tests, we do not find a significant cause for concern with using trained ML methods to predict our galaxy cluster masses when the underlying cosmological choices are different. This highlights the versatility of our chosen ML method. The ML method could be further diversified by including cluster measurements from a wide range of cosmological simulations (or observations) which, in affect, marginalizes over all the cosmological assumptions further reducing the dependence.

5 HETDEX AS A GALAXY CLUSTER SURVEY AT $Z < 0.5$

5.1 Constraints on Cosmological Parameters

Galaxy clusters are sensitive probes of Ω_m , the total mass ($\Omega_b + \Omega_c$) density in the universe, by tracing the peaks in the universal matter density often referred to as the power spectrum of matter density fluctuations or the matter power

spectrum and $\sigma_8 h^{-1}$, the normalization of the power spectrum, by the comparison of the number density of observed clusters to that predicted in cosmological models. Although, in reality, one measures $\sigma_8 h^{-1} \Omega_m^q$, where the value of q depends on the masses and redshifts of the halos considered.

To get a sense of how well HETDEX will be able to constrain cosmological parameters we follow the discussion of Weinberg et al. (2013) (hereafter W13), and begin with a few simplifying assumptions. While sensitive to Ω_m , the number density of clusters does not necessarily provide the strongest constraint, so we assume that some combination of other data sets (e.g., CMB, BAO, supernovae, WL, etc.) will constrain Ω_m to higher precision than is possible with clusters alone.

To estimate the error associated with a measurement of $\sigma_8 h^{-1}$ (which W13 refer to as $\sigma_{11,abs}$), W13 consider two sources of uncertainty, the systematic uncertainties in cluster mass calibration and the statistical uncertainty in the observed number density of clusters. The authors combine these two uncertainties though (their Eq. 141):

$$\Delta \ln \sigma_8 h^{-1}(z) \approx q(z) \times \max [\Delta \ln M, \alpha(z)^{-1} \Delta \ln N]. \quad (13)$$

where q is the degeneracy exponent between $\sigma_8 h^{-1}$ and Ω_m ,

Table 2. Scatter in cluster mass after bias correction for different bins of predicted cluster mass. This table shows the scatter in the predicted cluster mass for the perfect (top section), Targeted (middle section), and Survey (bottom section) observations in different predicted mass bins. The different mass recovery strategies are given in the leftmost column. It can be used to understand how the predicted cluster mass differs from the true cluster masses.

Method		Bins – Log M_{pred}							
		11.5 – 12	12 – 12.5	12.5 – 13	13 – 13.5	13.5 – 14	14 – 14.5	14.5 – 15	15 – 15.5
Perfect Observations									
Prob Based	Power Law	0.36 ± 0.07	0.39 ± 0.01	0.34 ± 0.00	0.22 ± 0.00	0.16 ± 0.00	0.14 ± 0.00	0.14 ± 0.01	0.11 ± 0.04
	σ	0.16 ± 0.03	0.24 ± 0.01	0.26 ± 0.00	0.20 ± 0.00	0.16 ± 0.00	0.14 ± 0.00	0.16 ± 0.01	0.19 ± 0.07
	σ, z	0.17 ± 0.03	0.21 ± 0.01	0.23 ± 0.00	0.19 ± 0.00	0.16 ± 0.00	0.55 ± 0.01	0.16 ± 0.01	0.39 ± 0.14
	σ, z, N_{gal}	0.10 ± 0.02	0.14 ± 0.01	0.47 ± 0.01	0.14 ± 0.00	0.10 ± 0.00	0.54 ± 0.01	1.62 ± 0.09	9.31 ± 3.38
ML Based	Power Law	0.36 ± 0.07	0.39 ± 0.01	0.34 ± 0.00	0.22 ± 0.00	0.16 ± 0.00	0.14 ± 0.00	0.14 ± 0.01	0.11 ± 0.04
	σ	0.22 ± 0.04	0.27 ± 0.01	0.29 ± 0.00	0.24 ± 0.00	0.21 ± 0.00	0.19 ± 0.00	0.18 ± 0.01	0.22 ± 0.08
	σ, z	0.19 ± 0.04	0.22 ± 0.01	0.25 ± 0.00	0.20 ± 0.00	0.18 ± 0.00	0.16 ± 0.00	0.17 ± 0.01	0.15 ± 0.05
	σ, z, N_{gal}	0.15 ± 0.03	0.18 ± 0.01	0.17 ± 0.00	0.14 ± 0.00	0.10 ± 0.00	0.08 ± 0.00	0.08 ± 0.00	0.10 ± 0.03
Targeted Observations									
Prob Based	Power Law	0.33 ± 0.07	0.41 ± 0.01	0.43 ± 0.01	0.39 ± 0.00	0.33 ± 0.00	0.27 ± 0.01	0.18 ± 0.01	0.11 ± 0.04
	σ	0.14 ± 0.03	0.19 ± 0.01	0.24 ± 0.00	0.25 ± 0.00	0.25 ± 0.00	0.22 ± 0.00	0.19 ± 0.01	0.30 ± 0.11
	σ, z	0.19 ± 0.04	0.20 ± 0.01	0.24 ± 0.00	0.24 ± 0.00	0.23 ± 0.00	0.56 ± 0.01	0.21 ± 0.01	0.36 ± 0.13
	σ, z, N_{gal}	0.14 ± 0.03	0.18 ± 0.01	0.20 ± 0.00	0.19 ± 0.00	0.17 ± 0.00	0.67 ± 0.01	2.28 ± 0.13	8.56 ± 3.11
ML Based	Power Law	0.33 ± 0.07	0.41 ± 0.01	0.43 ± 0.01	0.39 ± 0.00	0.33 ± 0.00	0.27 ± 0.01	0.18 ± 0.01	0.11 ± 0.04
	σ	0.29 ± 0.06	0.29 ± 0.01	0.31 ± 0.00	0.31 ± 0.00	0.32 ± 0.00	0.30 ± 0.01	0.29 ± 0.02	0.11 ± 0.04
	σ, z	0.14 ± 0.03	0.23 ± 0.01	0.26 ± 0.00	0.25 ± 0.00	0.24 ± 0.00	0.22 ± 0.00	0.25 ± 0.01	0.15 ± 0.05
	σ, z, N_{gal}	0.13 ± 0.03	0.21 ± 0.01	0.21 ± 0.00	0.18 ± 0.00	0.16 ± 0.00	0.14 ± 0.00	0.12 ± 0.01	0.15 ± 0.05
Survey Observations									
Prob Based	Power Law	0.16 ± 0.03	0.29 ± 0.01	0.33 ± 0.01	0.31 ± 0.01	0.25 ± 0.02	0.15 ± 0.06
	σ	0.11 ± 0.02	0.18 ± 0.01	0.22 ± 0.01	0.22 ± 0.01	0.19 ± 0.01	0.25 ± 0.09
	σ, z	0.13 ± 0.03	0.19 ± 0.01	0.22 ± 0.01	0.21 ± 0.01	1.31 ± 0.08	0.32 ± 0.11
	σ, z, N_{gal}	0.14 ± 0.03	0.18 ± 0.01	0.19 ± 0.01	0.19 ± 0.01	2.27 ± 0.15	9.19 ± 3.34
ML Based	Power Law	...	1.41 ± ...	0.40 ± 0.05	0.41 ± 0.02	0.38 ± 0.01	0.32 ± 0.01	0.25 ± 0.02	0.15 ± 0.06
	σ	...	0.30 ± ...	0.27 ± 0.03	0.28 ± 0.01	0.30 ± 0.01	0.30 ± 0.01	0.30 ± 0.02	0.29 ± 0.11
	σ, z	...	0.61 ± ...	0.22 ± 0.03	0.25 ± 0.01	0.25 ± 0.01	0.25 ± 0.01	0.25 ± 0.02	0.30 ± 0.11
	σ, z, N_{gal}	...	0.80 ± ...	0.19 ± 0.02	0.21 ± 0.01	0.20 ± 0.01	0.19 ± 0.01	0.19 ± 0.01	0.23 ± 0.08

$\Delta \ln M$ is the mass scale uncertainty, $\Delta \ln N$ is the cluster statistical uncertainty, and α is slope of the cumulative HMF. Using the [Tinker et al. \(2008\)](#) HMF at $z \sim 0.2$ and a limiting cluster mass of $10^{14} M_{\odot}$, [W13](#) estimate $q \sim 0.4$, $\alpha \sim 3$, and find that any cluster survey with more than 10-20 clusters is dominated by the uncertainty in the overall mass scale.

For a survey such as HETDEX, we can estimate the constraints on $\sigma_8 h^{-1}$ using Equation 13. Considering clusters with masses above $10^{14} M_{\odot}$, with Perfect knowledge, and the ML based cluster mass estimates the mass scale uncertainty (given in Table 2) is reduced to $\Delta_{log_{10}} M \sim 0.075$ dex or about 20%. This gives a uncertainty on $\sigma_8 h^{-1}$ of 7%. For clusters above $10^{14} M_{\odot}$, Survey observations can constrain the masses to about 51% which, in turn, constrains $\sigma_8 h^{-1}$ to 20%.

Because of the simplifying assumptions, and the superior quality of the data (no contamination, signal-to-noise issues, etc.), realistic expectations for HETDEX is to directly constrain $\sigma_8 h^{-1}$ to better precision than other methods (e.g., CMB, WL, X-ray) seems bleak. For example, [de Haan et al. \(2016\)](#) constrain $\sigma_8 h^{-1}$ to $\sim 5\%$ using a sample of 337 SZE detected clusters from the SPT-SZE survey. For the ~ 1500 clusters detected with Survey observations to con-

strain $\sigma_8 h^{-1}$ and to be dominated by cluster statistics alone ($\Delta \ln N \sim N^{-1/2}$), the absolute cluster calibration would need to be better than 2.5%. For a fully Targeted survey, about 14,000 clusters, this cluster mass calibration uncertainty reduces to $> 1\%$.

5.2 Calibration of the Richness-Cluster Mass Relation

Large-scale optical surveys (e.g., DES and LSST) expect to detect hundreds of thousands of galaxy clusters at $z < 1$. Because they produce photometry only, a major challenge for these surveys is relating a cluster observable to the total DM mass. One promising cluster mass estimator is the optical richness (e.g., [Abell 1958](#)). Specifically, here, we use λ , the weighted number of galaxies within a scale aperture (e.g., [Roza et al. 2011](#)) as calculated by the redMapper algorithm ([Rykoff et al. 2012](#)). Previous works (e.g., [Roza et al. 2010](#)) show that the richness correlates strongly with cluster mass on the average, but the absolute mass scale of the optical richness mass estimator and the scatter in cluster mass at fixed optical richness are imprecisely known ([Rykoff et al. 2012](#)). These systematics remain the major source of

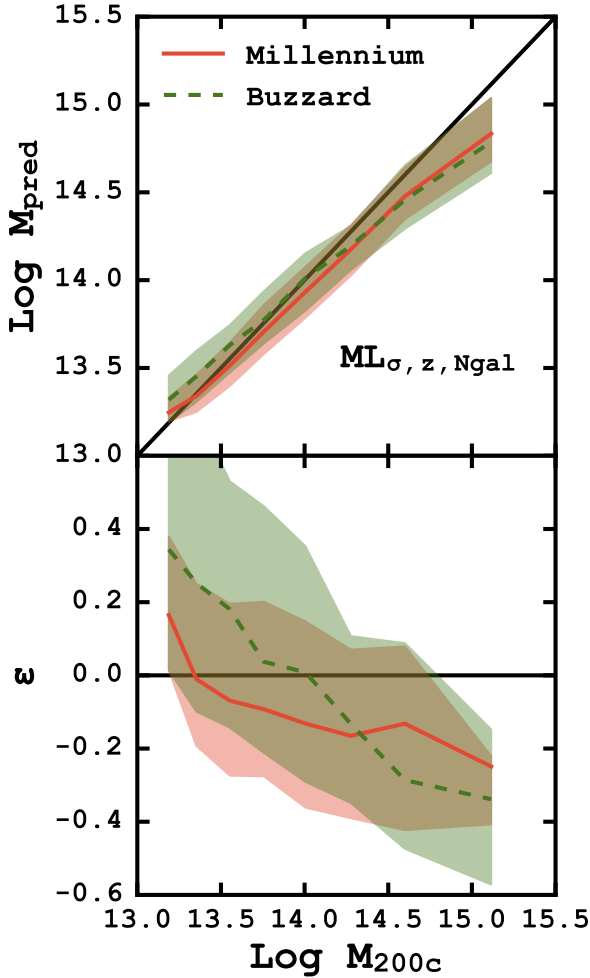


Figure 7. *Top:* ML based cluster mass predictions for the Millennium simulation clusters where the ML method has been trained with either a subset of the Millennium clusters (solid line) or the Buzzard catalog (dashed line). The shaded areas show the 68% scatter around the median. The solid black line shows the 1:1 relation. The solid black line shows the 1:1 relation. *Bottom:* The fractional error (Equation 12) also as a function of true cluster mass. The similarity of the predictions with the different training sets demonstrates how the ML method is not sensitive to the underlying cosmological assumptions.

uncertainty in deriving cosmological constraints from cluster abundances and must be measured using independent methods to realize the full potential of these types of surveys.

The Buzzard cluster catalogs do not contain measurements of λ , so we supplement it by generating richnesses based on the true cluster masses. For testing we assume two versions of the richness-mass relationship. Farahi et al. (2016) base the relation on stacked velocity dispersions, and Simet et al. (2016) use weak lensing measurements to construct their relation. Because we are investigating HETDEX’s ability to recover the overall cluster mass scale and underlying scatter in the mass-richness relationship, we use the true cluster masses perturbed by a known amount to estimate the observed richness.

To confirm that measuring the underlying scatter is possible, after generating richness values we calculate the scatter of the cluster masses at fixed λ , $\sigma_{M|\lambda}$, by comparing the true, unperturbed cluster masses against the richness and find that we do recover the expected scatter. We repeat the process with both assumed richness-mass relationships and recover the expected scatter in both instances.

Primarily, we are interested in the intrinsic scatter of the richness-mass relationship. This is because HETDEX is uniquely situated to estimate the scatter, whereas studies relying on stacked data (e.g., Farahi et al. 2016; Simet et al. 2016) lose that information. However, for technical reasons, we begin by estimating how well HETDEX will constrain the absolute mass scale (something stacked studies excel at). As part of our fitting process to constrain the mass scale, we estimate the overall scatter in the relationship, so it makes sense to begin here.

To get an idea of how well HETDEX will constrain the absolute mass scale, we can find the best fitting relation to our richness-mass data. To generate the best fitting lines we follow the general procedure of Hogg et al. (2010), by defining an objective function and then minimizing the loss. Our objective function is

$$p(y_i|x_i, \sigma_{y_i}, m, b, \sigma) = \frac{1}{\sqrt{2\pi(\sigma_{y_i}^2 + \sigma^2)}} \exp\left(-\frac{[y_i - m x_i - b]^2}{2(\sigma_{y_i}^2 + \sigma^2)}\right) \quad (14)$$

where y_i is the observed cluster mass, x_i is the observed richness, σ_{y_i} is the uncertainty in observed cluster mass, m is the power law slope, b is the overall cluster mass scale, and σ is the intrinsic scatter between richness and cluster mass. We assume that the intrinsic scatter is constant from point to point and that all of the measurement errors are Gaussian. We convert this objective function into a likelihood by multiplying all of the individual probabilities together,

$$\mathcal{L} = \prod_{i=1}^N p(y_i|x_i, \sigma_{y_i}, m, b, \sigma). \quad (15)$$

We again rely on MCMC samples to sample the posterior probability distribution and thus maximize the likelihood. The best fitting slope and intercept are quoted as the median value of the posterior probability distribution with 68% error bars defined as the second moment of the same distribution.

We limit our clusters to those with $10 \leq \lambda < 130$ in our fitting analysis because there are very few clusters with $\lambda > 130$ and to better coincide with other observational studies (e.g., Saro et al. 2015) which have lower limits on λ . For a richness-mass relation with an intrinsic scatter of $\langle \sigma_{M|\lambda} \rangle = 0.25$ dex, we find a best-fitting relation for the Targeted observations as

$$\text{Log } M_{200c}/M_{\odot} = 12.54 \pm 0.02 + 0.97 \pm 0.02 \text{ Log } \lambda \quad (16)$$

and the Survey observations as

$$\text{Log } M_{200c}/M_{\odot} = 12.78 \pm 0.04 + 0.86 \pm 0.03 \text{ Log } \lambda \quad (17)$$

This gives $M_{200c} = (1.22 \pm \dots) \times 10^{14} M_{\odot}$ and $M_{200c} = (1.44 \pm \dots) \times 10^{14} M_{\odot}$ at $\lambda = 40$ for the Targeted and Survey observations respectively. In both cases, this normalization differs significantly from the $M_{200c} \approx 2.1 \times 10^{14} h^{-1} M_{\odot}$ found in recent work Li et al. (2016); Simet et al. (2016).

If the intrinsic scatter is reduced to ~ 0.05 dex we recover an overall normalization of $M_{200c} = (1.8 \pm \dots) \times 10^{14} M_{\odot}$ and $M_{200c} = (1.78 \pm \dots) \times 10^{14}$ for the Targeted and Survey observations at $\lambda = 40$.

The intrinsic scatter is also estimated during the fitting process. For observations with a richness-mass relation intrinsic scatter of $\langle \sigma_{M|\lambda} \rangle = 0.25$ dex, we recover $\langle \sigma_{M|\lambda} \rangle = 0.22 \pm 0.003$ dex and $\langle \sigma_{M|\lambda} \rangle = 0.20 \pm 0.01$ dex for Targeted and Survey observations respectively. The discrepancy between the intrinsic value and the measured value is due to the uncertainties in the individual cluster mass predictions. As the prediction intervals are narrowed, the recovered intrinsic scatter approaches the true value. For example, with cluster mass prediction intervals half the size of the current intervals we measure $\langle \sigma_{M|\lambda} \rangle$ to be ~ 0.25 and ~ 0.23 for the two sets of observations.

Figure 8 summarizes the main results of this investigation. The top panel shows the generated optical richness, λ , versus the predicted cluster mass. The cluster masses are the $ML_{\sigma,z,N_{gal}}$ based and correspond to the Targeted and Survey observation strategies. The bottom panel of Figure 8 shows the scatter in the predicted cluster masses at fixed richness, $\sigma_{M|\lambda}$. The solid line represents the intrinsic amount of scatter added to the masses. The cluster masses are binned in increasing ten richness intervals (10–20, 20–30, etc.). The inset upper panel shows the intrinsic scatter versus the recovered average scatter at fixed richness, $\langle \sigma_{M|\lambda} \rangle$ and illustrates how well the two observation strategies recover the intrinsic scatter.

We find that we are able to accurately recover an average intrinsic scatter of $0.2 < \langle \sigma_{M|\lambda} \rangle < 0.3$ dex, finding $\langle \sigma_{M|\lambda} \rangle = 0.255 \pm 0.02$ at $\sigma_{true} = 0.25$ with Survey observations. This is very promising as other observational studies have estimated the intrinsic scatter of real clusters to be ~ 0.25 dex (e.g., [Rozo & Rykoff 2014](#); [Rozo et al. 2015](#)). As the intrinsic scatter increases or decreases, we fail to recover the scatter as accurately.

For

6 SUMMARY

Here, we present detailed simulations of the upcoming HETDEX survey’s applicability to the detection and total mass measurement of galaxy clusters. We use mock galaxy catalogs, and simulated, HETDEX-like observational strategies to estimate the number of clusters observed and the precision of their total mass estimates, using three different cluster mass estimators. We discuss HETDEX’s ability to constrain the cosmological parameter $\sigma_8 h^{-1}$ and comment on how HETDEX may improve current and future photometric large-area sky surveys’ cluster mass estimates derived from optical richness.

Our main conclusions are the following:

(i) We find approximately 14000 clusters with at least five cluster members in the HETDEX cluster survey volume. Of those, approximately 1500 clusters are detected with HETDEX-like survey observations. The number of cluster members recovered is almost exactly 4.5 times fewer than a fully Targeted survey, across both a wide range of redshifts and cluster masses.

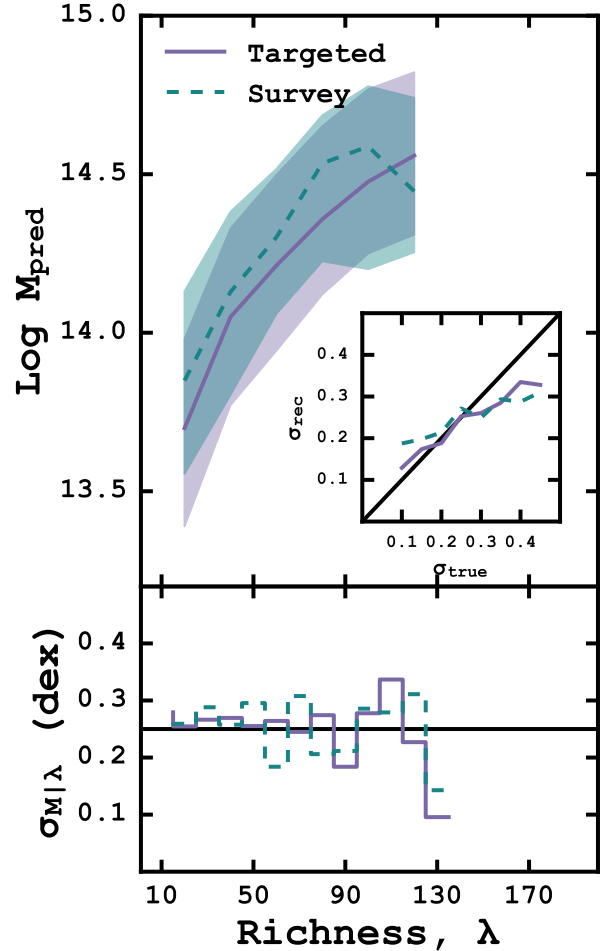


Figure 8. *Top:* The optical richness, λ , versus the predicted cluster mass. The solid, colored line is the median predicted mass for the Targeted observing, and the colored, dashed line is the median recovered mass for the HETDEX-like observations. The shaded regions represent the 68% scatter around the median values. *Bottom:* The scatter in the relation at fixed richness. The solid black line shows the intrinsic scatter of $\sigma_{true} = 0.25$ dex. Color coding is the same as the top panel. *Inset:* The evolution of the intrinsic scatter versus the average recovered scatter, σ_{rec} . We find good agreement when intrinsic scatter is ~ 0.25 dex.

(ii) Overall, we find a traditional power law conversion from LOSVD to cluster mass performs significantly poorer than either the probability based or ML based methods also tested. The probability based and ML based cluster mass estimators are able to more accurately predict cluster mass when combined with information other than just the LOSVD. While the power law may be outperformed, overall, comparisons of similar mass galaxy clusters shows that above $\text{Log } M/M_{\odot} = 14.5$, the power law gives a lower bias than either the probability based or ML based methods. For HETDEX-like observations and clusters with $13 < \text{Log } M/M_{\odot} < 14.5$, we find the $ML_{\sigma,z,N_{gal}}$ method performs the best. Below $\text{Log } M/M_{\odot} = 13$ no method with Survey observations gives an bias of less than 50%.

(iii) For followup Targeted observations only galaxy clus-

ters with masses inferred to be $\text{Log } M/M_{\odot} < 13$ from Survey observations should be targeted. Galaxy clusters with inferred masses below $\text{Log } M/M_{\odot} = 13$ can see as much as an 81% improvement in cluster mass estimation with Targeted observations. While the improvement of clusters with masses above $\text{Log } M/M_{\odot} = 13$ is often approximately 10%.

(iv) For a cluster survey limited to $M > 10^{14} M_{\odot}$ HETDEX's ability to constrain the cosmological parameter $\sigma_8 h^{-1}$ is at best $\sim 20\%$. This is significantly different than recent constraints from SZE surveys.

(v) HETDEX will be able to place important constraints on the amount of scatter in the optical richness-mass relationship. It will to a less extent constrain the overall normalization of the relation. This should provide an important too in the calibration of large-area sky surveys which rely on photometric data only to estimate cluster masses.

It is the author's hope that this work may be useful to others when conducting their own research. Because this work relies heavily on (often) complex data analysis, and in order to promote transparency and reproducible science, we provide all of the code used to conduct this study at <https://github.com/boada/desCluster>. Regrettably, large file size prevents including the source data with the analysis routines. The authors are happy to provide them, if requested.

ACKNOWLEDGEMENTS

The authors also wish to thank the anonymous referee whose comments and suggestions significantly improved both the quality and clarity of this work. We also thank Steven W. Crawford for many helpful discussions. This research made use of This research made use of the IPYTHON package (Perez & Granger 2007) and MATPLOTLIB, a Python library for publication quality graphics (Hunter 2007). Figure 3 is heavily based on Foreman-Mackey et al. (2016). Funding for the SDSS and SDSS-II has been provided by the Alfred P. Sloan Foundation, the Participating Institutions, the National Science Foundation, the U.S. Department of Energy, the National Aeronautics and Space Administration, the Japanese Monbukagakusho, the Max Planck Society, and the Higher Education Funding Council for England. The SDSS Web Site is <http://www.sdss.org/>.

REFERENCES

- Abell G. O., 1958, *ApJS*, 3, 211
- Acquaviva V., 2016, *MNRAS*, 456, 1618
- Acquaviva V., Gawiser E., Leung A. S., Martin M. R., 2014, *Proc. IAU*, 10, 365
- Alam S., et al., 2015, *ApJS*, 219, 12
- Baxter E. J., Rozo E., Jain B., Rykoff E., Wechsler R. H., 2016, eprint arXiv:1604.00048, p. 7
- Beers T. C., Flynn K., Gebhardt K., 1990, *AJ*, 100, 32
- Behroozi P. S., Wechsler R. H., Wu H.-Y., 2013, *ApJ*, 762, 109
- Boada S., 2016, *MNRAS*
- Bocquet S., et al., 2015, *ApJ*, 799, 214
- Carlstrom J. E., Holder G. P., Reese E. D., 2002, *Annu. Rev. Astron. Astrophys.*, 40, 643
- Carlstrom J. E., et al., 2011, *PASP*, 123, 568
- Caruana R., Niculescu-Mizil A., 2006, in Proc. 23rd Int. Conf. Mach. Learn. - ICML '06. ACM Press, New York, New York, USA, pp 161–168, doi:10.1145/1143844.1143865, <http://portal.acm.org/citation.cfm?doid=1143844.1143865>
- Chabrier G., 2003, *PASP*, 115, 763
- Colless M., et al., 2001, *MNRAS*, 328, 1039
- Crocce M., Pueblas S., Scoccimarro R., 2006, *MNRAS*, 373, 369
- Croton D. J., et al., 2006, *MNRAS*, 365, 11
- De Lucia G., Blaizot J., 2007, *MNRAS*, 375, 2
- De Lucia G., Springel V., White S. D. M., Croton D., Kauffmann G., 2006, *MNRAS*, 366, 499
- Eisenstein D. J., et al., 2005, *ApJ*, 633, 560
- Evrard A. E., et al., 2008, *ApJ*, 672, 122
- Farahi A., Evrard A. E., Rozo E., Rykoff E. S., Wechsler R. H., 2016, eprint arXiv:1601.05773
- Foreman-Mackey D., Hogg D. W., Lang D., Goodman J., 2013, *PASP*, 125, 306
- Foreman-Mackey D., et al., 2016,] 10.5281/zenodo.45906
- Goodman J., Weare J., 2010, *Commun. Appl. Math. Comput. Sci.*, 5, 65
- Hill G. J., et al., 2008, Panor. Views Galaxy Form. Evol. ASP Conf. Ser., 399
- Hill G. J., et al., 2012, in McLean I. S., Ramsay S. K., Takami H., eds, Vol. 8446, Ground-based Airborne Instrum. Astron. IV. Proc. SPIE. p. 84460N, doi:10.1117/12.925434, <http://adsabs.harvard.edu/abs/2012SPIE.8446E..0NH>
- Hogg D., 1999, Arxiv Prepr. astro-ph/9905116, 1, 1
- Hogg D. W., Bovy J., Lang D., 2010, eprint arXiv:1008.4686
- Hunter J. D., 2007, *Comput. Sci. Eng.*, 9, 90
- Kelz A., et al., 2014, in Ramsay S. K., McLean I. S., Takami H., eds, Vol. 9147, Proc. SPIE. p. 914775, doi:10.1117/12.2056384, <http://adsabs.harvard.edu/abs/2014SPIE.9147E..75K>
- Kirk B., et al., 2015, *MNRAS*, 449, 4010
- LSST Dark Energy Science Collaboration 2012, arXiv Prepr. arXiv:1211.0310, p. 133
- Lemson G., The Virgo Consortium 2006, eprint arXiv:astro-ph/0608019
- Li R., et al., 2016, *MNRAS*, 458, 2573
- Mantz A., Allen S. W., Rapetti D., Ebeling H., 2010, *MNRAS*, 406, no
- Mantz A. B., Allen S. W., Morris R. G., Schmidt R. W., von der Linden A., Urban O., 2015, *MNRAS*, 449, 199
- Meinshausen N., 2006, J. Mach. Learn. Res., 7, 983
- Milvang-Jensen B., et al., 2008, *A&A*, 482, 419
- Munari E., Biviano A., Borgani S., Murante G., Fabjan D., 2013, *MNRAS*, 430, 2638
- Murray S., Power C., Robotham A., 2013, *Astron. Comput.*, 3-4, 23
- Neal R. M., 1997, Technical Report 9722, Markov Chain Monte Carlo Methods Based on 'Slicing' the Density Function, <http://citeseerx.ist.psu.edu/viewdoc/download?doi=10.1.1.48.886{&}rep=rep1{&}type=pdf>. Department of Statistics, University of Toronto, Toronto, doi:10.1.1.48.886, <http://citeseerx.ist.psu.edu/viewdoc/download?doi=10.1.1.48.886{&}rep=rep1{&}type=pdf>
- Ntampaka M., Trac H., Sutherland D. J., Battaglia N., Póczos B., Schneider J., 2015a, eprint arXiv:1509.05409
- Ntampaka M., Trac H., Sutherland D. J., Battaglia N., Póczos B., Schneider J., 2015b, *ApJ*, 803, 50
- Oke J. B., 1974, *ApJS*, 27, 21
- Pedregosa F., et al., 2012, J. Mach. Learn. Res., 12, 2825
- Perez F., Granger B. E., 2007, *Comput. Sci. Eng.*, 9, 21
- Planck Collaboration 2013, *A&A*, 571, 19
- Reddick R. M., Wechsler R. H., Tinker J. L., Behroozi P. S., 2013, *ApJ*, 771, 30
- Ripley B. D., 2007, Pattern recognition and neural networks. Cambridge university press

- Robotham A. S. G., et al., 2011, *MNRAS*, 416, 2640
- Rozo E., Rykoff E. S., 2014, *ApJ*, 783, 80
- Rozo E., et al., 2010, *ApJ*, 708, 645
- Rozo E., Wu H.-Y., Schmidt F., 2011, *ApJ*, 735, 118
- Rozo E., Rykoff E. S., Bartlett J. G., Melin J.-B., 2015, *MNRAS*, 450, 592
- Ruel J., et al., 2014, *ApJ*, 792, 45
- Rykoff E. S., et al., 2012, *ApJ*, 746, 178
- Rykoff E. S., et al., 2014, *ApJ*, 785, 104
- Saro A., Mohr J. J., Bazin G., Dolag K., 2013, *ApJ*, 772, 47
- Saro A., et al., 2015, *MNRAS*, 454, 2305
- Sehgal N., et al., 2011, *ApJ*, 732, 44
- Sifón C., et al., 2013, *ApJ*, 772, 25
- Sifón C., et al., 2015a, eprint arXiv:1512.00910
- Sifón C., Hoekstra H., Cacciato M., Viola M., Köhlinger F., van der Burg R. F. J., Sand D. J., Graham M. L., 2015b, *A&A*, 575, A48
- Simet M., McClintock T., Mandelbaum R., Rozo E., Rykoff E., Sheldon E., Wechsler R. H., 2016, eprint arXiv:1603.06953
- Spergel D. N., et al., 2003, *ApJS*, 148, 175
- Springel V., 2005, *MNRAS*, 364, 1105
- Springel V., et al., 2005, *Nature*, 435, 629
- Sunyaev R. A., Zeldovich Y. B., 1972, *Comments Astrophys. Sp. Phys.*, 4
- Swetz D. S., et al., 2011, *ApJS*, 194, 41
- The Dark Energy Survey Collaboration 2005, eprint arXiv:astro-ph/0510346, p. 42
- Tin Kam Ho 1995, in *Proc. 3rd Int. Conf. Doc. Anal. Recognit.. IEEE Comput. Soc. Press*, pp 278–282, doi:10.1109/ICDAR.1995.598994, <http://ieeexplore.ieee.org/lpdocs/epic03/wrapper.htm?arnumber=598994>
- Tin Kam Ho 1998, *IEEE Trans. Pattern Anal. Mach. Intell.*, 20, 832
- Tinker J., Kravtsov A. V., Klypin A., Abazajian K., Warren M., Yepes G., Gottlöber S., Holz D. E., 2008, *ApJ*, 688, 709
- Turner E. L., Gott, J. R. I., 1976, *ApJS*, 32, 409
- Vanderlinde K., et al., 2010, *ApJ*, 722, 1180
- Weinberg D. H., Mortonson M. J., Eisenstein D. J., Hirata C., Riess A. G., Rozo E., 2013, *Phys. Rep.*, 530, 87
- Xu X., Ho S., Trac H., Schneider J., Poczós B., Ntampaka M., 2013, *ApJ*, 772, 147
- de Haan T., et al., 2016, eprint arXiv:1603.06522
- van der Burg R. F. J., Muzzin A., Hoekstra H., Wilson G., Lidman C., Yee H. K. C., 2014, *A&A*, 561, A79

This paper has been typeset from a $\text{\TeX}/\text{\LaTeX}$ file prepared by the author.